Solving Multi-Resolution Quantitative Inverse Scattering Problems Through the *IMSA-NIE* Method

M. Salucci, A. Polo, and A. Massa

Abstract

The Iterative Multi-Scaling Approach (*IMSA*) is a well-known recipe to counteract the *non-linearity* and *ill-posedness* of an inverse scattering (*IS*) problem. As a matter of fact, it allows to keep as low as possible the ratio between problem unknowns and non-redundant/informative data. In this way, the occurrence of local minima (i.e., false solutions of the *IS* problem) is limited with respect to standard (single-resolution) approaches. Moreover, it exploits *progressively-acquired* information on the unknown targets, acting *de facto* as an effective regularization tool. In this work, the *IMSA* is integrated with a New Integral Equation (*NIE*) method, with the goal of further mitigating the non-linearity of the *IS* problem and enable the robust quantitative imaging of quite string scatterers under non-negligible levels of noise on processed data. Numerical results are shown to verify the effectiveness of the integrated *IMSA-NIE* approach when dealing with the challenging problem of imaging disconnected scatterers with conductivities different from the surrounding medium (i.e., free-space).

Contents

1 List of Symbols

- $k = \frac{2\pi}{\lambda}$: Free-space wave-number;
- D: Investigation domain;
- L_D: Side of the investigation domain;
- $a = L_D\frac{\sqrt{2}}{2}$: Radius of the smallest circle containing D;
- $\mathbf{r} = (x, y)$: Position vector;
- $\tau(\mathbf{r})$: Contrast function;
- $\varepsilon_r(\mathbf{r})$: Relative permittivity;
- ε_0: Free-space permittivity;
- $\sigma(\mathbf{r})$: Conductivity;
- Ξ: Reconstruction error;
- V: Number of views/sources;
- φ^v: Direction of the v-th plane wave ($v = 1, ..., V$);
- M: Number of measurement points;
- ρ: Radius of the measurement domain;
- N: Number of discretization cells inside D;
- Γ: Number of degrees-of-freedom of the scattered field;
- U: Number of retrievable unknowns;
- η: $IMSA$ Stopping threshold;
- S: Maximum number of $IMSA$ iterations;
- $L^{(s)}$: Side of the region of interest (RoI) at the s-th $IMSA$ step ($s = 1, ..., S$);
- K: Number of singular values used by the SOM to retrieve the minimum-norm currents;
- α: Threshold for the adaptive selection of the number of singular values;
- χ_m: m-th Singular value of the scattering operator ($m = 1, ..., M$);
- MF: Number of Fourier bases;
- β: NIE regularization parameter;
- γ: Multiplicative factor for the adaptive computation of β;
- I: Number of iterations;

2 Numerical Results

2.1 "Double I" Profile - Variation of SNR and σ_{obj}

Investigation domain (D)

- Side: $L_D = 3.0$ [λ];

Measurement setup

- Views
  - Type: plane wave with unitary magnitude;
  - Frequency: $f = 300$ [MHz];
  - Wavelength: $\lambda = 1.0$ [m];
  - Number of $DOFs$: $\Gamma = 2ka = 2k\left(L_D\frac{\sqrt{2}}{2}\right) = 4\frac{\pi}{\lambda}\left(L_D\frac{\sqrt{2}}{2}\right) \simeq 26.64$;
  - Number of views: $V = 27$;
  - Direction: $\varphi_v = (v-1)\,\frac{360}{V}$; $v = 1, ..., V$;
- Measurement points
  - Radius: $\rho = a = \left(L_D\frac{\sqrt{2}}{2}\right) = 2.12$ [λ];
  - Number of probes: $M = 27$;
  - Location: $(x_m,\, y_m) = \left(\rho\cos\left((m-1)\,\frac{2\pi}{M}\right),\, \rho\sin\left((m-1)\,\frac{2\pi}{M}\right)\right)$; $m = 1, ..., M$;

Scatterer

- Type: "Double I" Profile
- Dielectric characteristics:

$\varepsilon_{r,obj}$	σ_{obj} [S/m]	$\Re\{\tau\}$	$\Im\{\tau\}$
2.0	0.0	1.0	0.0
2.0	10^{-4}	1.0	-0.006
2.0	10^{-3}	1.0	-0.060
2.0	10^{-2}	1.0	-0.6

Table I: "Austria" Profile - Considered contrasts.

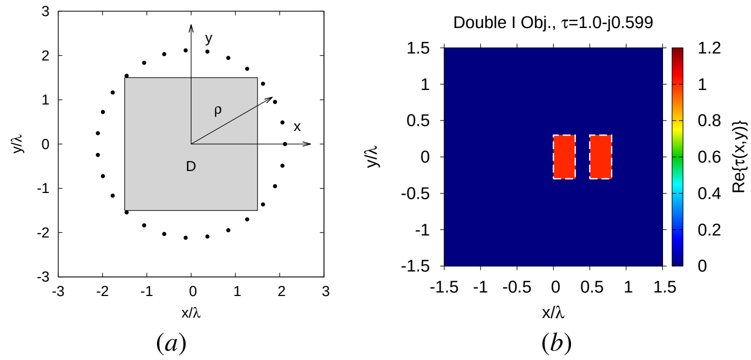

(a) (b)

Figure 1: "Double I" Profile, $\tau = 1.0 - j0.6$ - (a) Imaging scenario and (b) actual dielectric profile.

Forward solver (MoM)

- Discretization: $N^{fwd} = 60 \times 60 = 3600$;
- Side of each cell: $l^{fwd} \simeq 0.05$ $[\lambda]$;

Inverse solver

1. $IMSA - SOM - NIE$

   - Number of retrievable unknowns: $U = \frac{(2ka)^2}{2} = 4\pi^2 \left(\frac{L}{\lambda}\right)^2 = 355$;
   - Discretization: $N^{IMSA} = 18 \times 18 = 324$;
   - Side of each cell @ $s = 1$: $l_{s=1} = 0.17$ $[\lambda]$;
   - Maximum number of steps: $S = 4$;
   - $IMSA$ stop criterion: adaptive ($\eta = 0.2$);
   - Selection of the singular values: adaptive;
   - Threshold for the adaptive selection of the number of singular values: $\alpha = 0.4$ (calibrated);
   - Number of Fourier bases: $MF = \frac{\sqrt{N^{IMSA}}}{2} = 9$ (standard SOM);
   - Selection of the NIE regularization parameter: adaptive;
   - Multiplicative factor for the selection of the NIE regularization parameter: $\gamma = 0.5$ (calibrated);
   - Number of iterations: $I = 100$.

2. $BARE - SOM - NIE$

   - Discretization: $N^{BARE} = 30 \times 30 = 900$;
   - Side of each cell: $l = 0.1$ $[\lambda]$;
   - Number of singular values: $K = 15$ (non-adaptive);
   - Number of Fourier bases: $MF = \frac{\sqrt{N^{BARE}}}{2} = 15$ (standard SOM);
   - NIE regularization parameter: $\beta = 2.0$ (non-adaptive, calibrated);

- Number of iterations: $I = 100$.

3. $IMSA-SOM-CSI$

   - Same parameters of $IMSA-SOM-NIE$;
   - Threshold for the adaptive selection of the number of singular values: $\alpha = 0.7$;

4. $BARE-SOM-CSI$

   - Same parameters of $BARE-SOM-NIE$;

Signal to noise ratio

- $SNR = \{10;\ 20;\ 40; 60\}$ [dB].

2.1.1 $\varepsilon_r = 2.0, \sigma = 0.0$ [S/m] $\rightarrow \tau = 1.0$

$IMSA - SOM - NIE$ **vs.** $BARE - SOM - NIE$: **Final reconstructions**

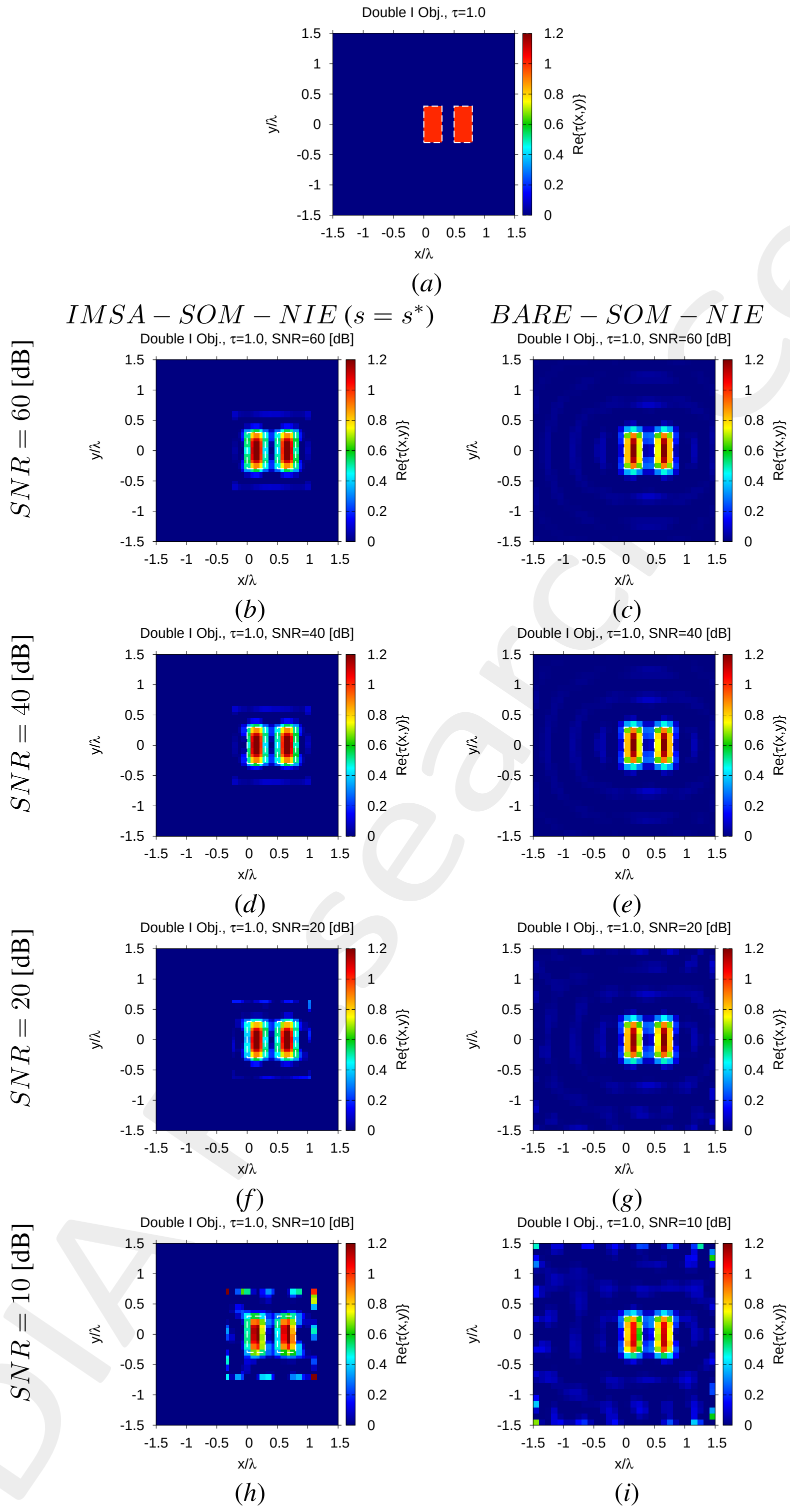

Figure 2: "Double I" Profile, $\tau = 1.0$ - (a) Actual and (b)-(i) retrieved contrast by the $IMSA - SOM - NIE$ and $BARE - SOM - NIE$ methods under several noise levels.

$IMSA - SOM - NIE$: Intermediate Reconstructions

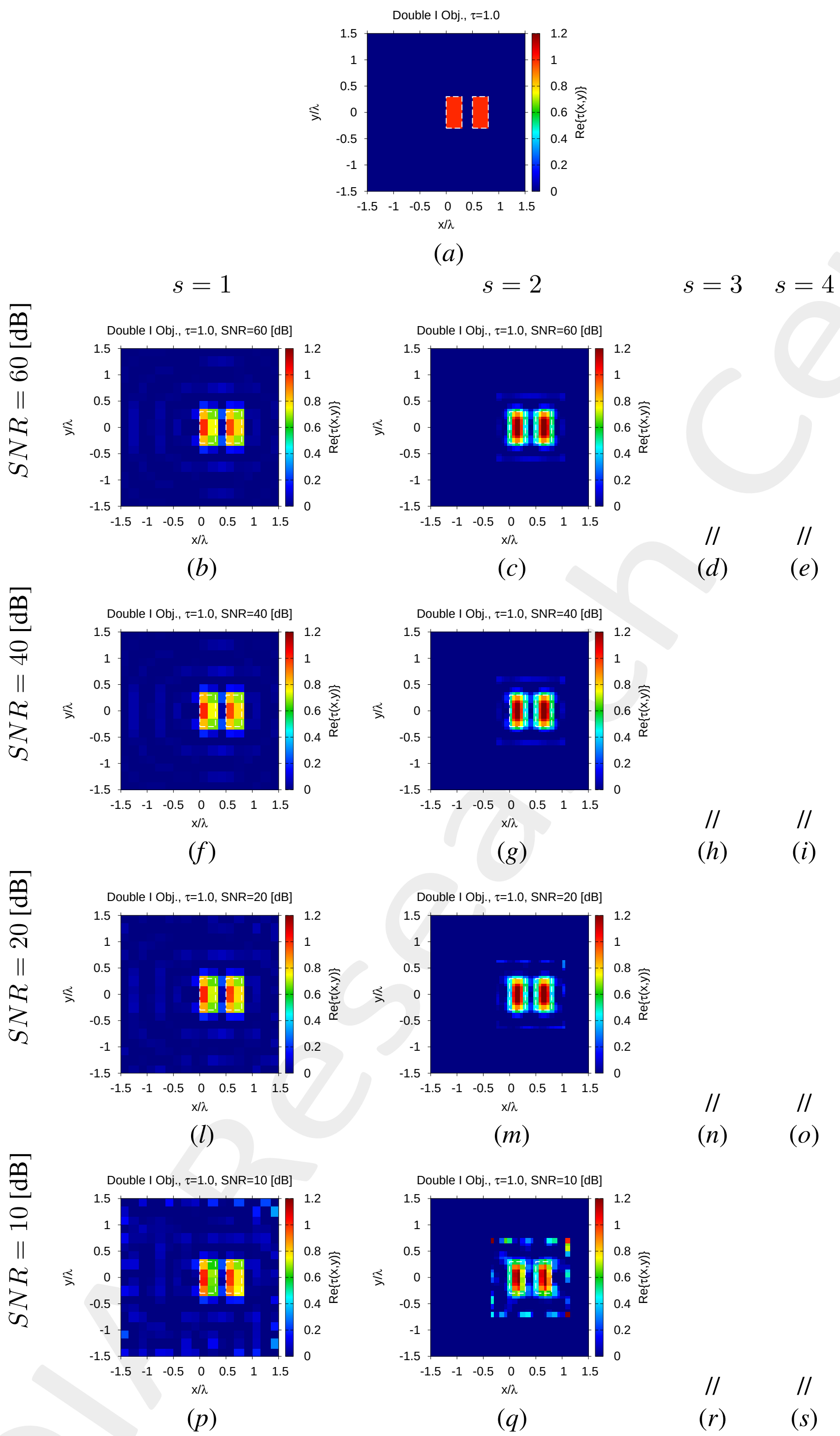

Figure 3: "Double I" Profile, $\tau = 1.0$ - (a) Actual and (b)-(i) intermediate retrieved contrast by the $IMSA-SOM-NIE$ under several noise levels.

$IMSA-SOM-CSI$ vs. $BARE-SOM-CSI$: Final reconstructions

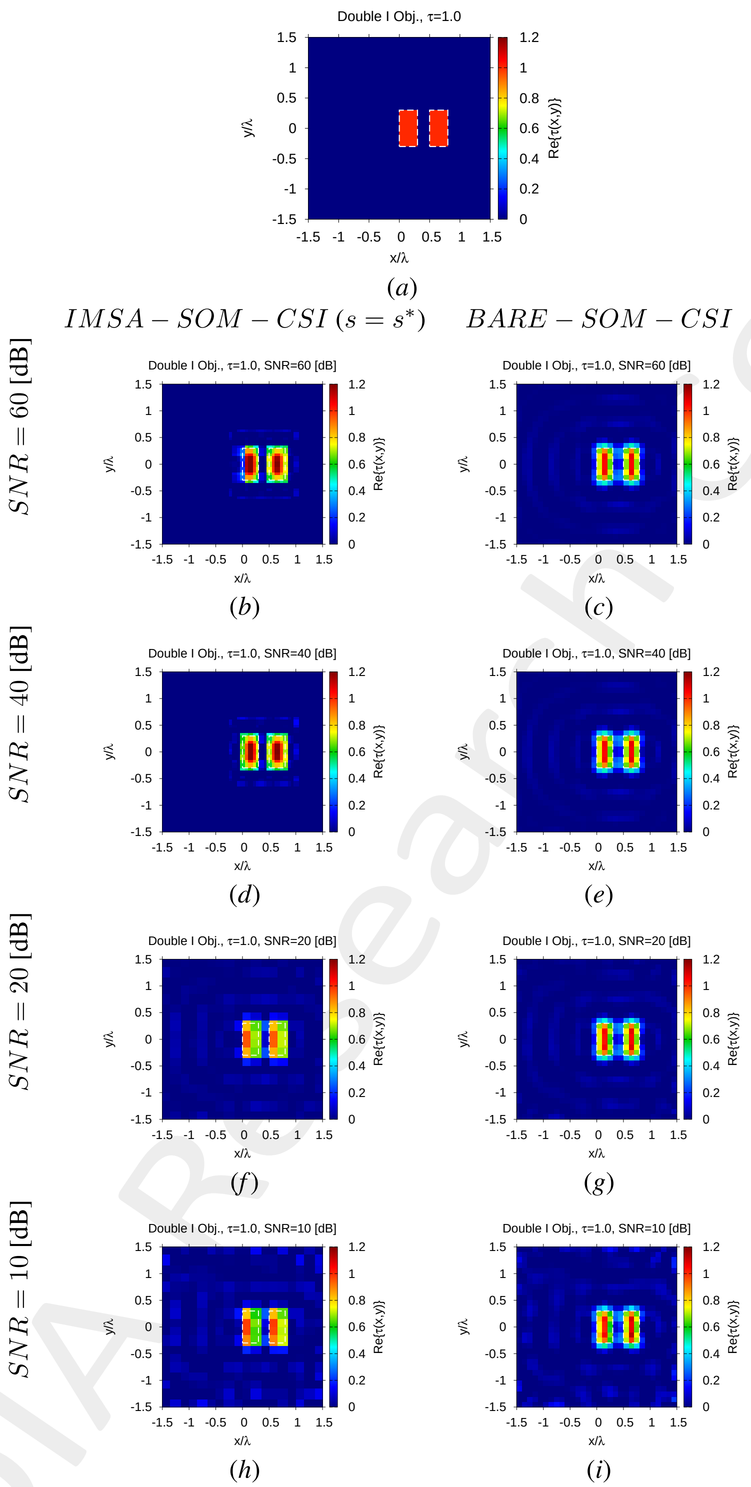

Figure 4: "Double I" Profile, $\tau = 1.0$ - (a) Actual and (b)-(i) retrieved contrast by the $IMSA-SOM-CSI$ and $BARE-SOM-CSI$ methods under several noise levels.

Reconstruction Errors vs. SNR

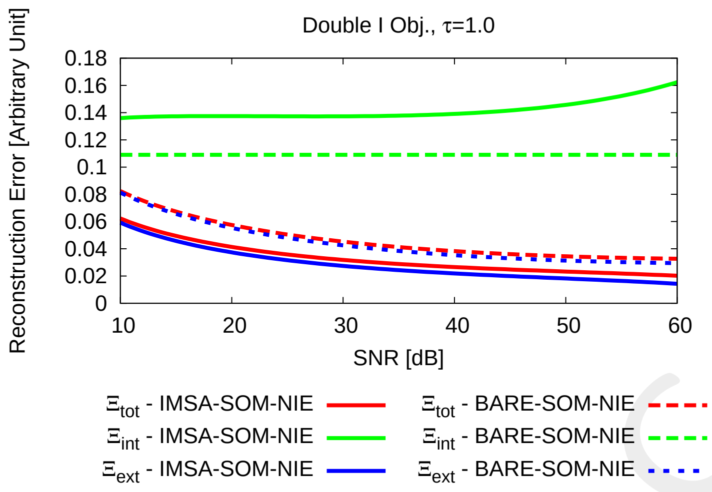

Figure 5: "Double I" Profile, $\tau = 1.0$- Reconstruction errors for the $IMSA-SOM-NIE$ and $BARE-SOM-NIE$ methods.

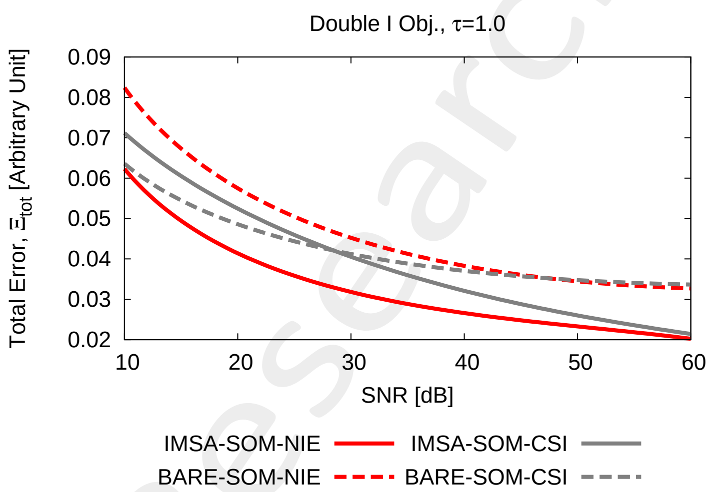

Figure 6: "Double I" Profile, $\tau = 1.0$ - Total error for $IMSA - SOM - NIE$, $BARE - SOM - NIE$, $IMSA - SOM - CSI$, and $BARE - SOM - CSI$.

2.1.2 $\varepsilon_r = 2.0, \sigma = 10^{-4}$ [S/m] $\rightarrow \tau = 1.0 - j0.006$

$IMSA - SOM - NIE$ **vs.** $BARE - SOM - NIE$**: Final reconstructions (Real Part)**

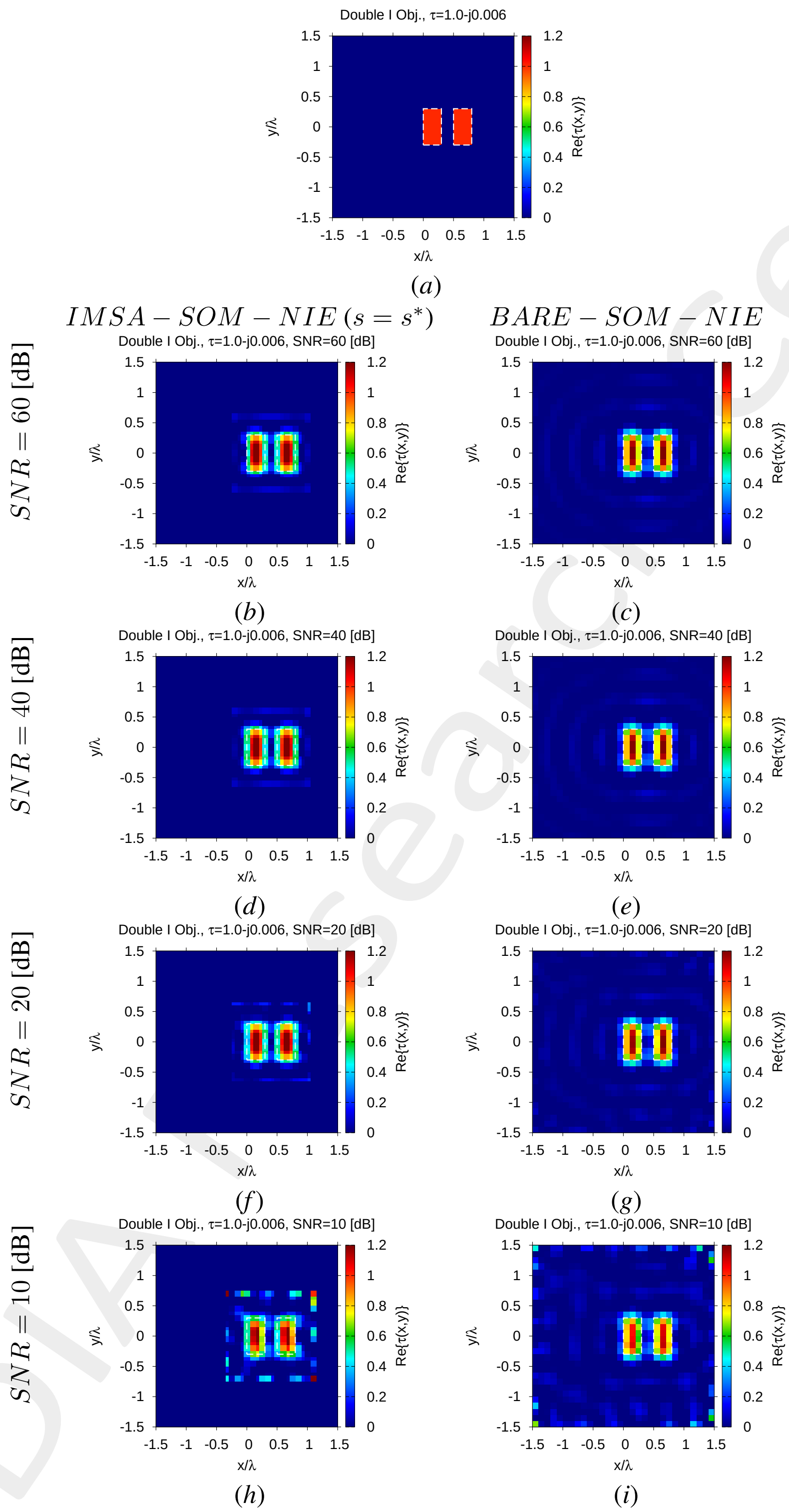

Figure 7: "Double I" Profile, $\tau = 1.0 - j0.006$ - (a) Actual and (b)-(i) retrieved contrast by the $IMSA - SOM - NIE$ and $BARE - SOM - NIE$ methods under several noise levels.

$IMSA-SOM-NIE$ vs. $BARE-SOM-NIE$: **Final reconstructions (Imaginary Part)**

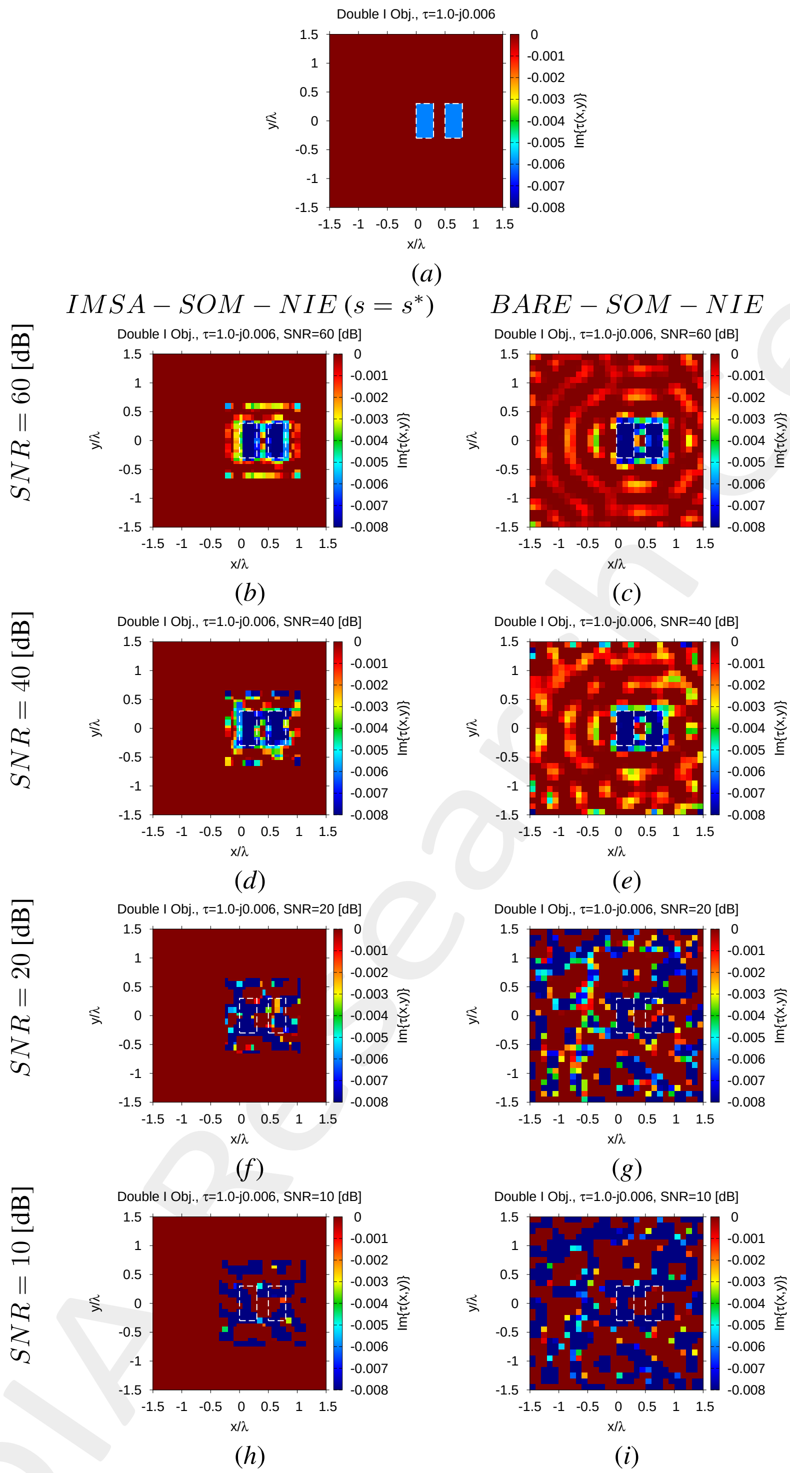

Figure 8: "Double I" Profile, $\tau = 1.0 - j0.006$ - (a) Actual and (b)-(i) retrieved contrast (imaginary part) by the $IMSA-SOM-NIE$ and $BARE-SOM-NIE$ methods under several noise levels.

$IMSA-SOM-CSI$ vs. $BARE-SOM-CSI$: Final reconstructions (Real Part)

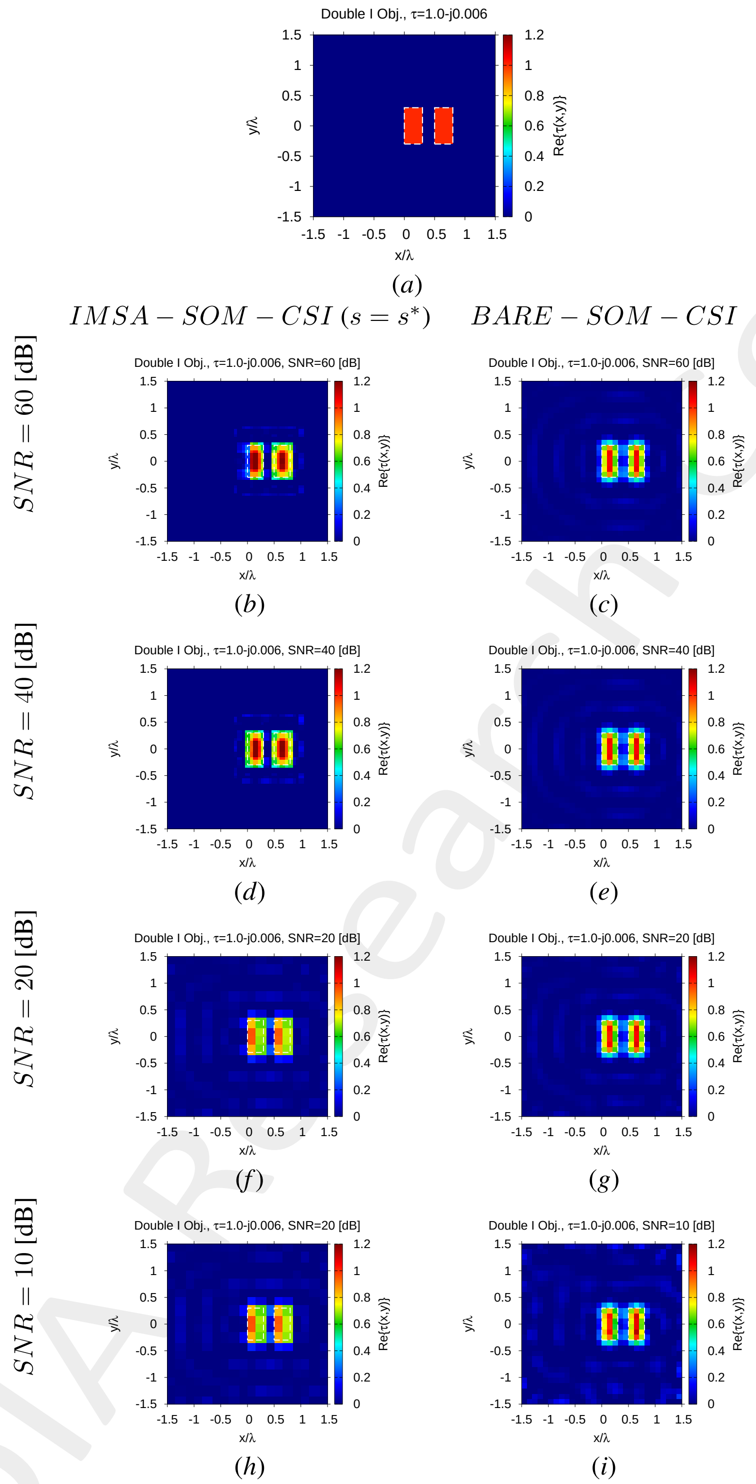

Figure 9: "Double I" Profile, $\tau=1.0-j0.006$ - (a) Actual and (b)-(i) retrieved contrast by the $IMSA-SOM-CSI$ and $BARE-SOM-CSI$ methods under several noise levels.

$IMSA-SOM-CSI$ **vs.** $BARE-SOM-CSI$**: Final reconstructions (Imaginary Part)**

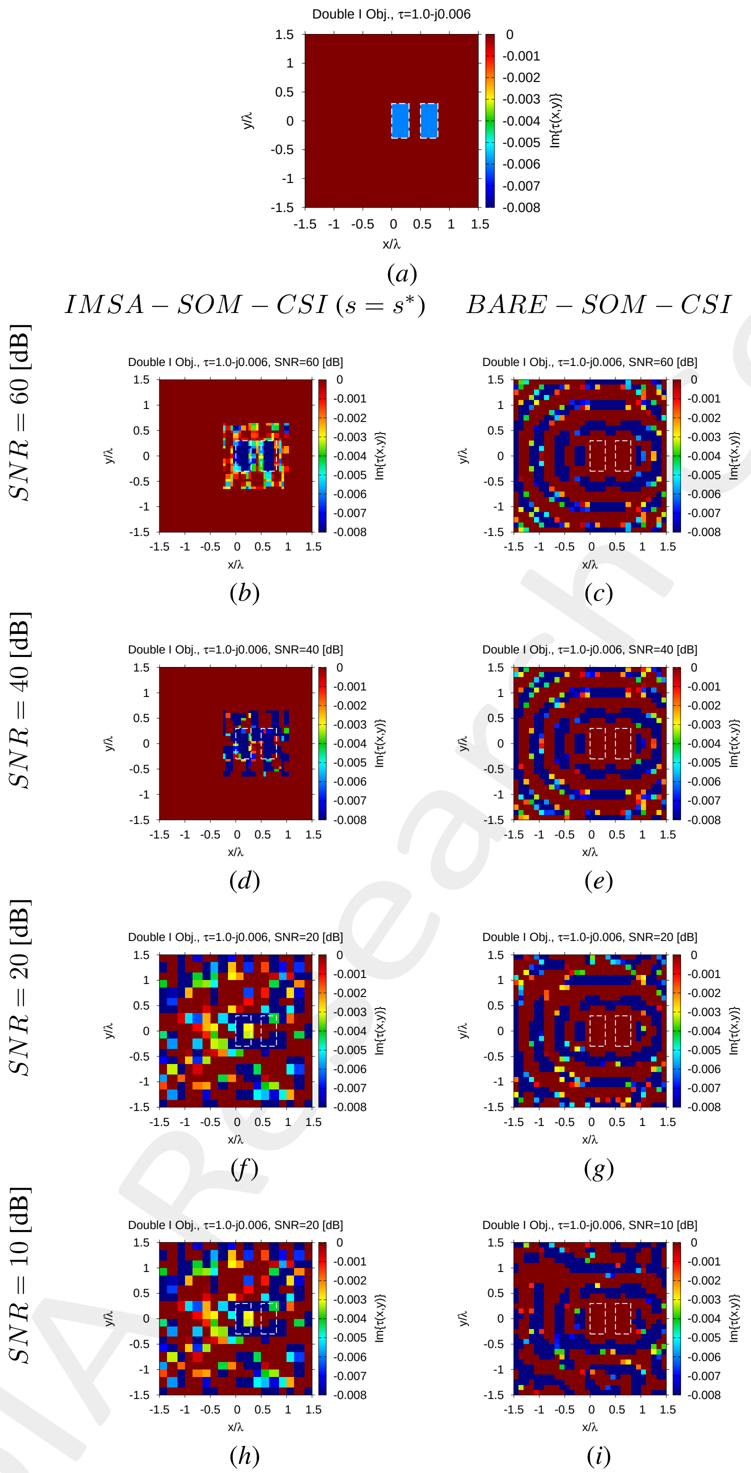

Figure 10: "Double I" Profile, $\tau = 1.0 - j0.006$ - (a) Actual and (b)-(i) retrieved contrast by the $IMSA-SOM-CSI$ and $BARE-SOM-CSI$ methods under several noise levels.

Reconstruction Errors vs. SNR

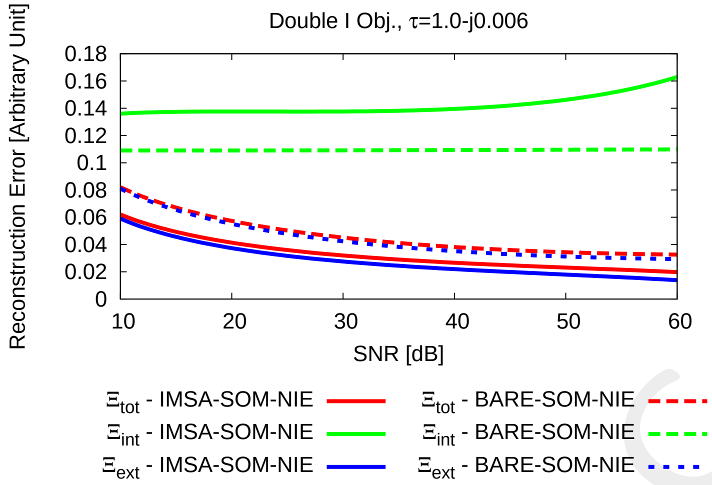

Figure 11: "Double I" Profile, $\tau = 1.0 - j0.006$ - Reconstruction errors for the $IMSA - SOM - NIE$ and $BARE - SOM - NIE$ methods.

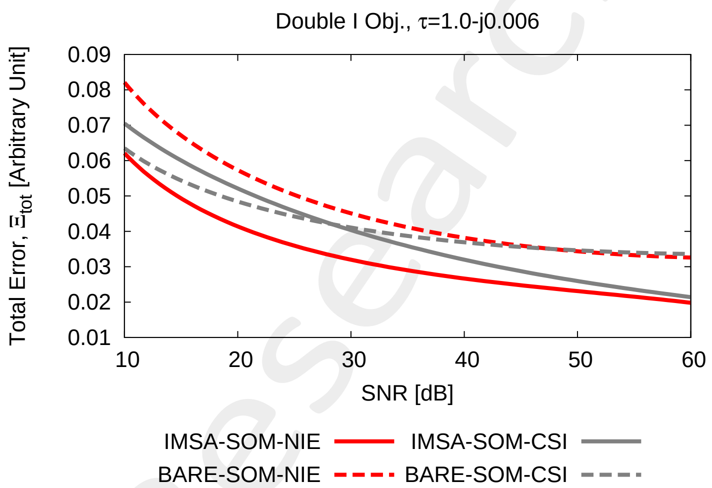

Figure 12: "Double I" Profile, $\tau = 1.0 - j0.006$ - Total error for $IMSA - SOM - NIE$, $BARE - SOM - NIE$, $IMSA - SOM - CSI$, and $BARE - SOM - CSI$.

2.1.3 $\varepsilon_r = 2.0$, $\sigma = 10^{-3}$ [S/m] $\rightarrow \tau = 1.0 - j0.06$

$IMSA - SOM - NIE$ **vs.** $BARE - SOM - NIE$**: Final reconstructions (Real Part)**

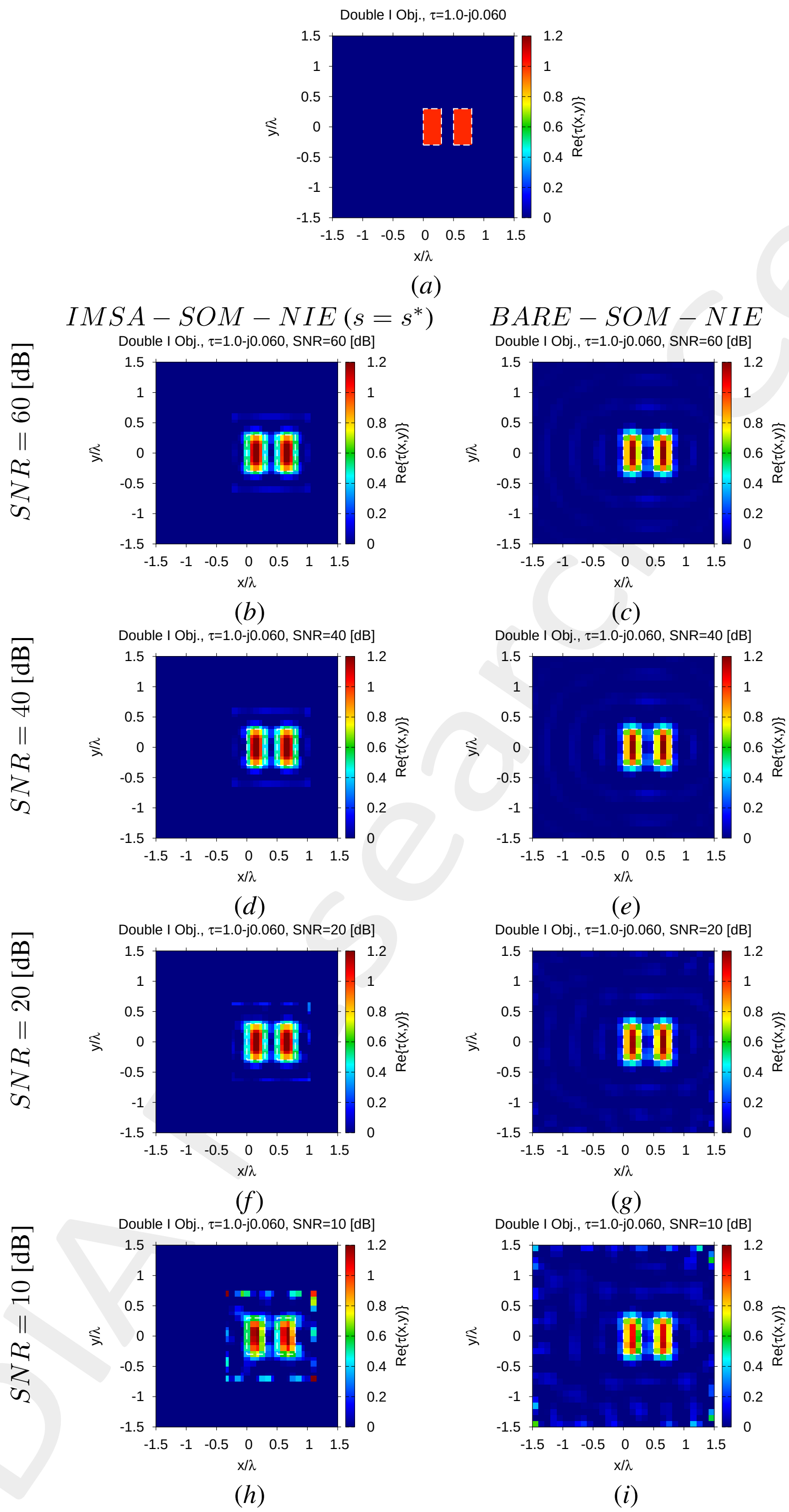

Figure 13: "Double I" Profile, $\tau = 1.0 - j0.06$ - (a) Actual and (b)-(i) retrieved contrast by the $IMSA - SOM - NIE$ and $BARE - SOM - NIE$ methods under several noise levels.

$IMSA-SOM-NIE$ **vs.** $BARE-SOM-NIE$**: Final reconstructions (Imaginary Part)**

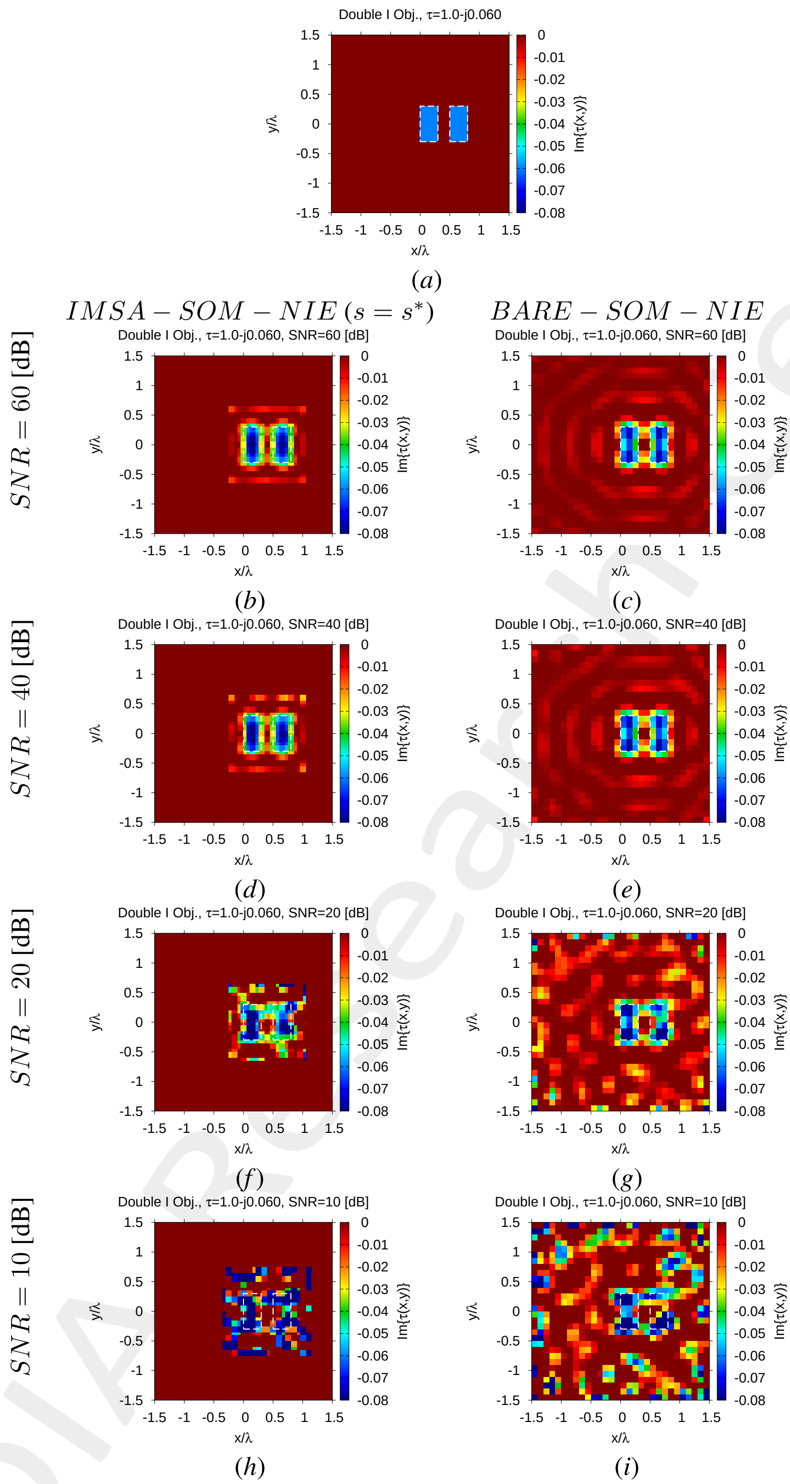

Figure 14: "Double I" Profile, $\tau = 1.0 - j0.06$ - (a) Actual and (b)-(i) retrieved contrast (imaginary part) by the $IMSA-SOM-NIE$ and $BARE-SOM-NIE$ methods under several noise levels.

$IMSA-SOM-CSI$ **vs.** $BARE-SOM-CSI$**: Final reconstructions (Real Part)**

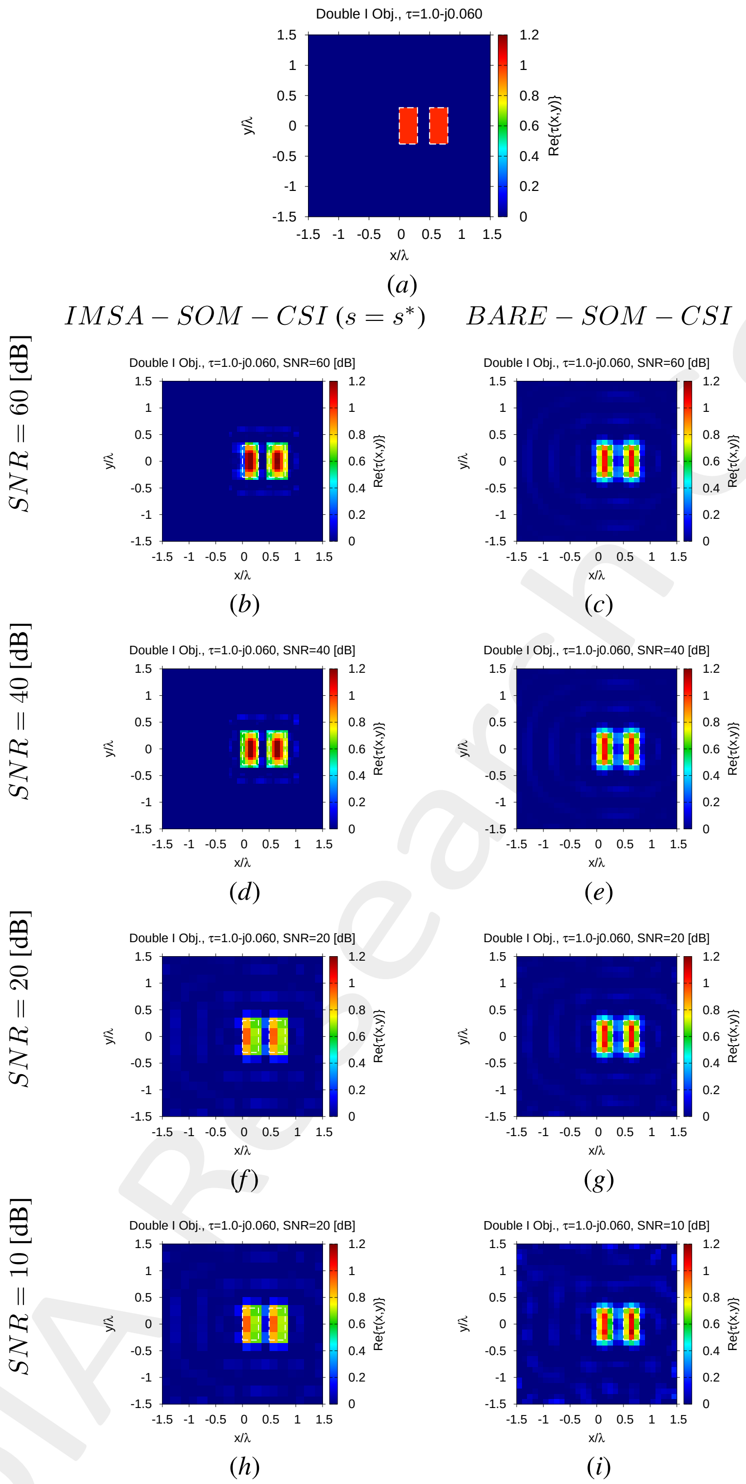

Figure 15: “Double I” Profile, $\tau = 1.0 - j0.06$ - (a) Actual and (b)-(i) retrieved contrast by the $IMSA-SOM-CSI$ and $BARE-SOM-CSI$ methods under several noise levels.

$IMSA-SOM-CSI$ **vs.** $BARE-SOM-CSI$**: Final reconstructions (Imaginary Part)**

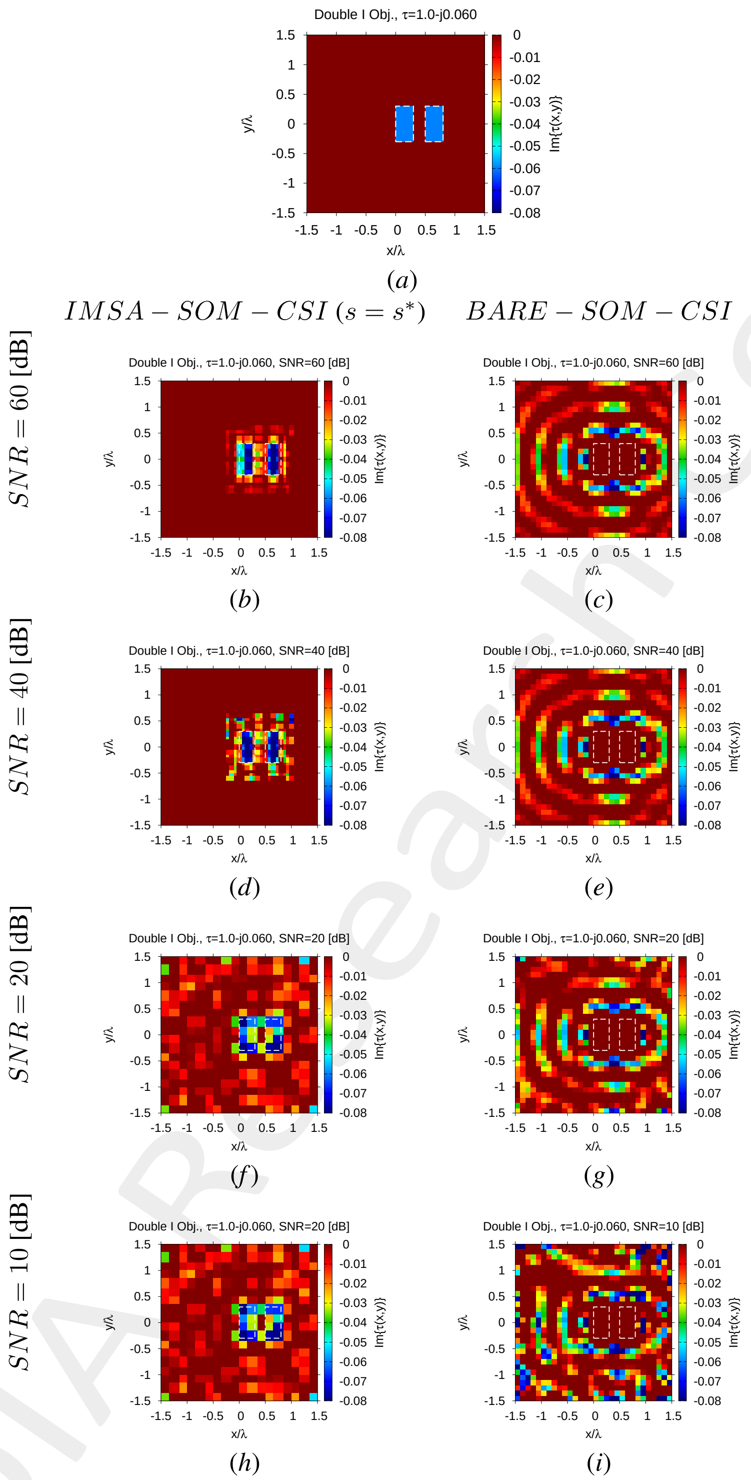

Figure 16: "Double I" Profile, $\tau = 1.0 - j0.06$ - (a) Actual and (b)-(i) retrieved contrast (imaginary part) by the $IMSA-SOM-CSI$ and $BARE-SOM-CSI$ methods under several noise levels.

Reconstruction Errors vs. SNR

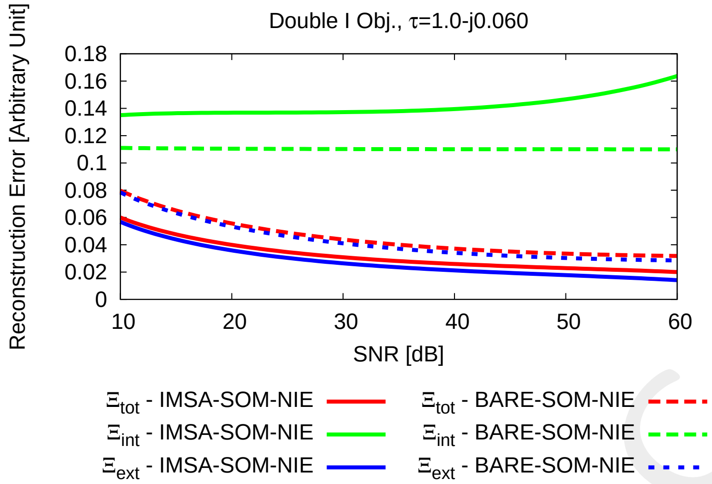

Figure 17: "Double I" Profile, $\tau = 1.0 - j0.06$ - Reconstruction errors for the $IMSA - SOM - NIE$ and $BARE - SOM - NIE$ methods.

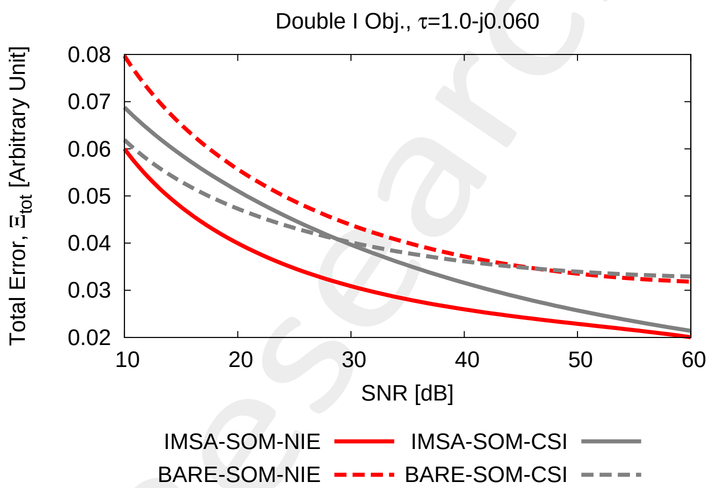

Figure 18: "Double I" Profile, $\tau = 1.0 - j0.06$ - Total error for $IMSA - SOM - NIE$, $BARE - SOM - NIE$, $IMSA - SOM - CSI$, and $BARE - SOM - CSI$.

2.1.4 $\varepsilon_r = 2.0$, $\sigma = 10^{-2}$ [S/m] $\rightarrow \tau = 1.0 - j0.6$

$IMSA - SOM - NIE$ **vs.** $BARE - SOM - NIE$**: Final reconstructions (Real Part)**

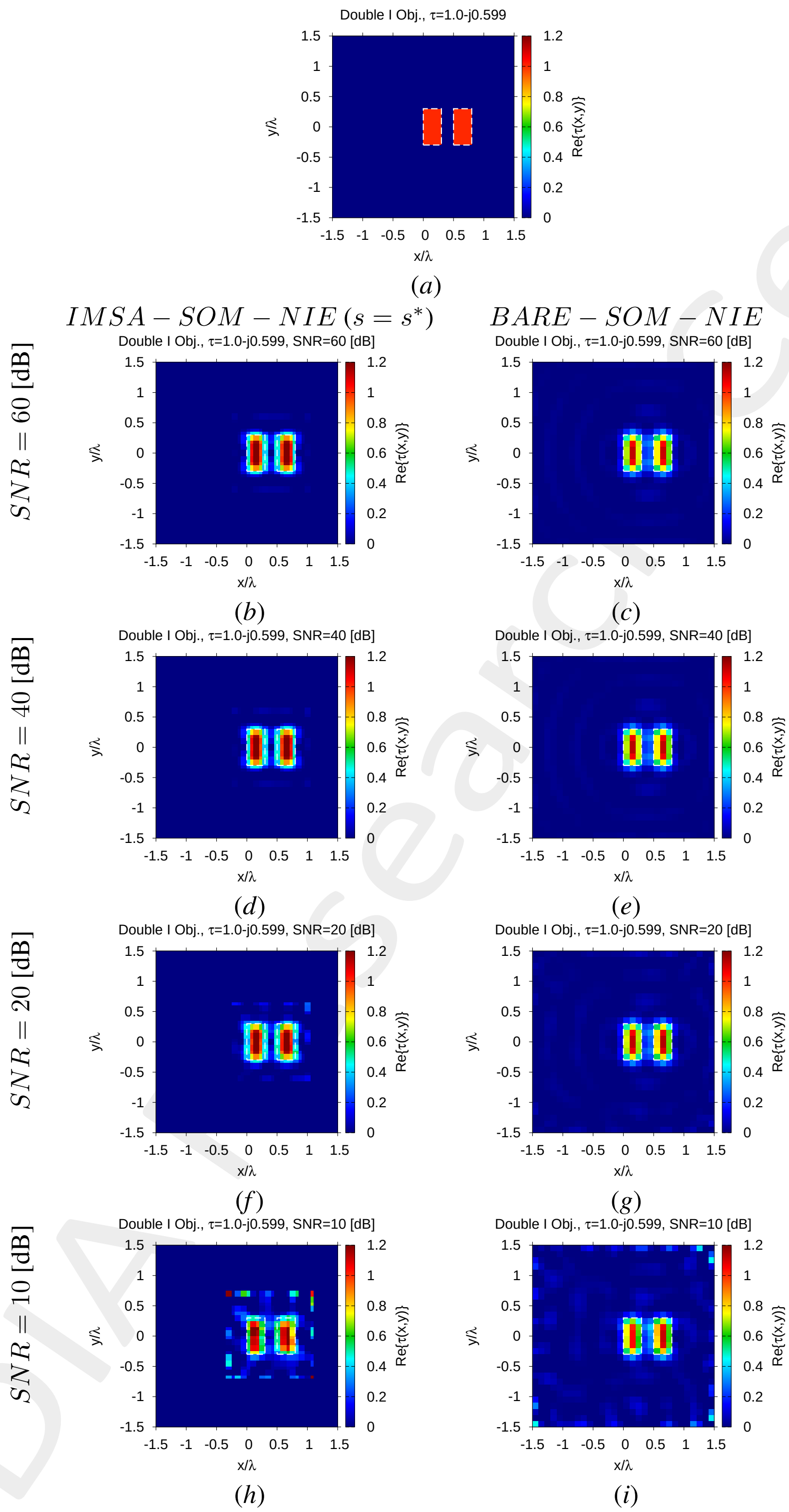

Figure 19: "Double I" Profile, $\tau = 1.0 - j0.6$ - (a) Actual and (b)-(i) retrieved contrast by the $IMSA - SOM - NIE$ and $BARE - SOM - NIE$ methods under several noise levels.

$IMSA - SOM - NIE$ **vs.** $BARE - SOM - NIE$**: Final reconstructions (Imaginary Part)**

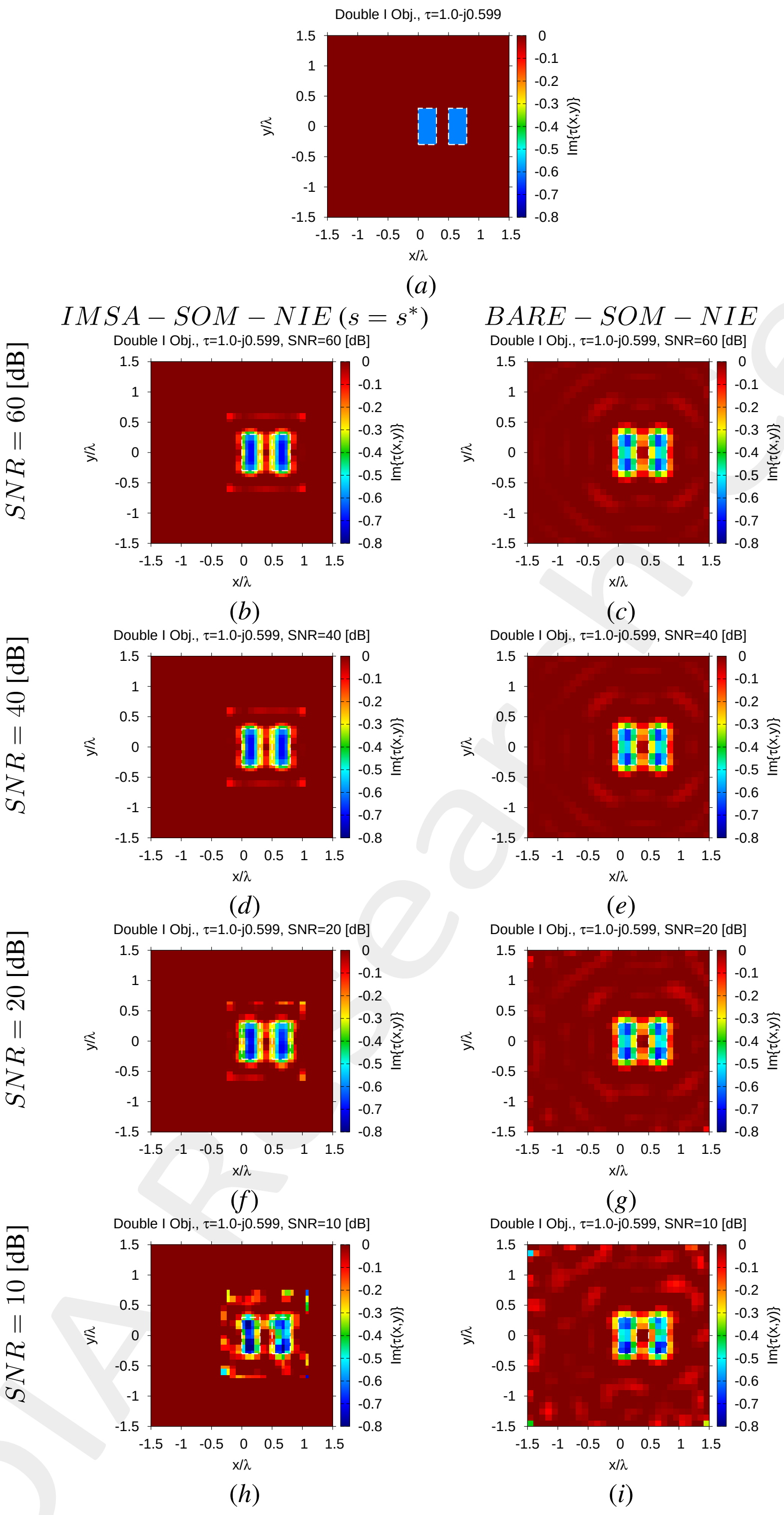

Figure 20: "Double I" Profile, $\tau = 1.0 - j0.6$ - (a) Actual and (b)-(i) retrieved contrast (imaginary part) by the $IMSA - SOM - NIE$ and $BARE - SOM - NIE$ methods under several noise levels.

$IMSA - SOM - CSI$ **vs.** $BARE - SOM - CSI$**: Final reconstructions (Real Part)**

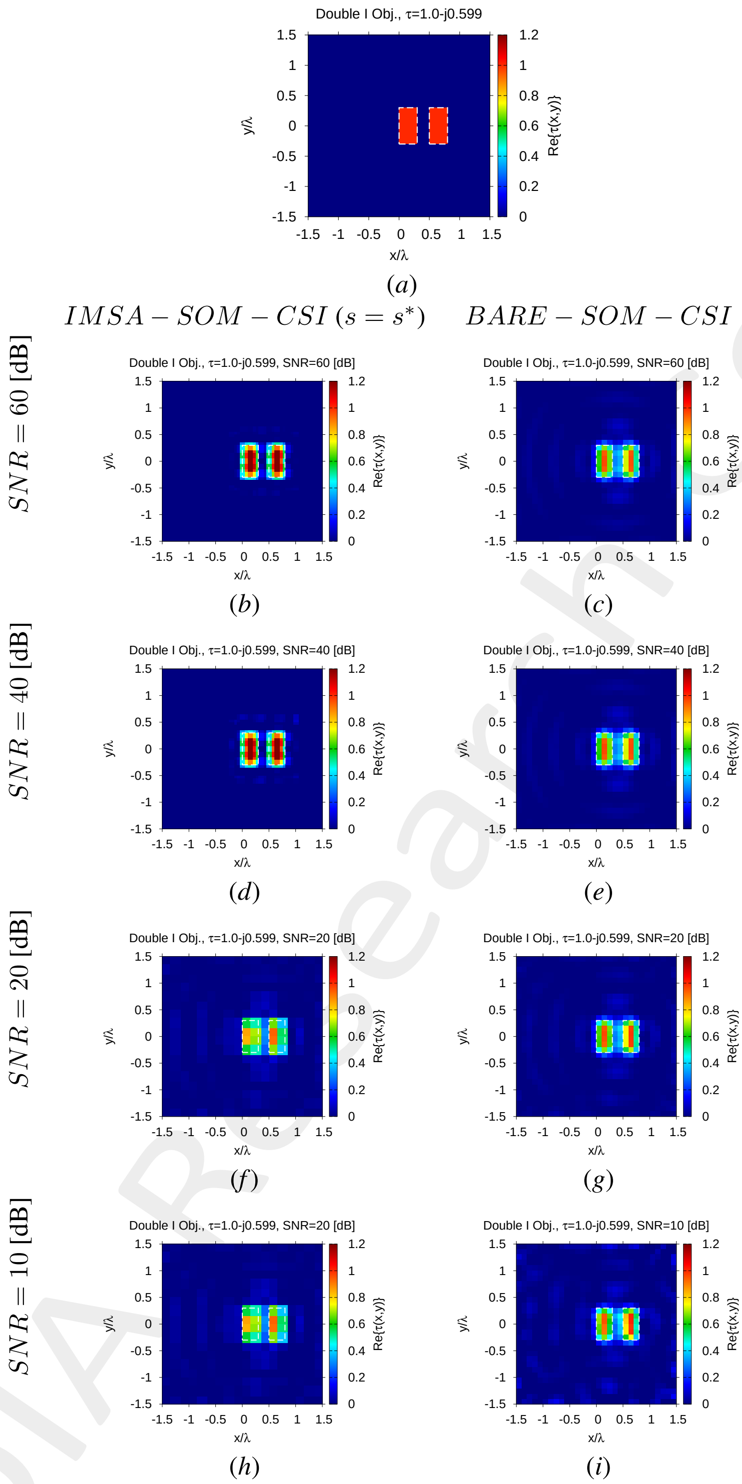

Figure 21: "Double I" Profile, $\tau = 1.0 - j0.6$ - (a) Actual and (b)-(i) retrieved contrast by the $IMSA - SOM - CSI$ and $BARE - SOM - CSI$ methods under several noise levels.

$IMSA-SOM-CSI$ vs. $BARE-SOM-CSI$: Final reconstructions (Imaginary Part)

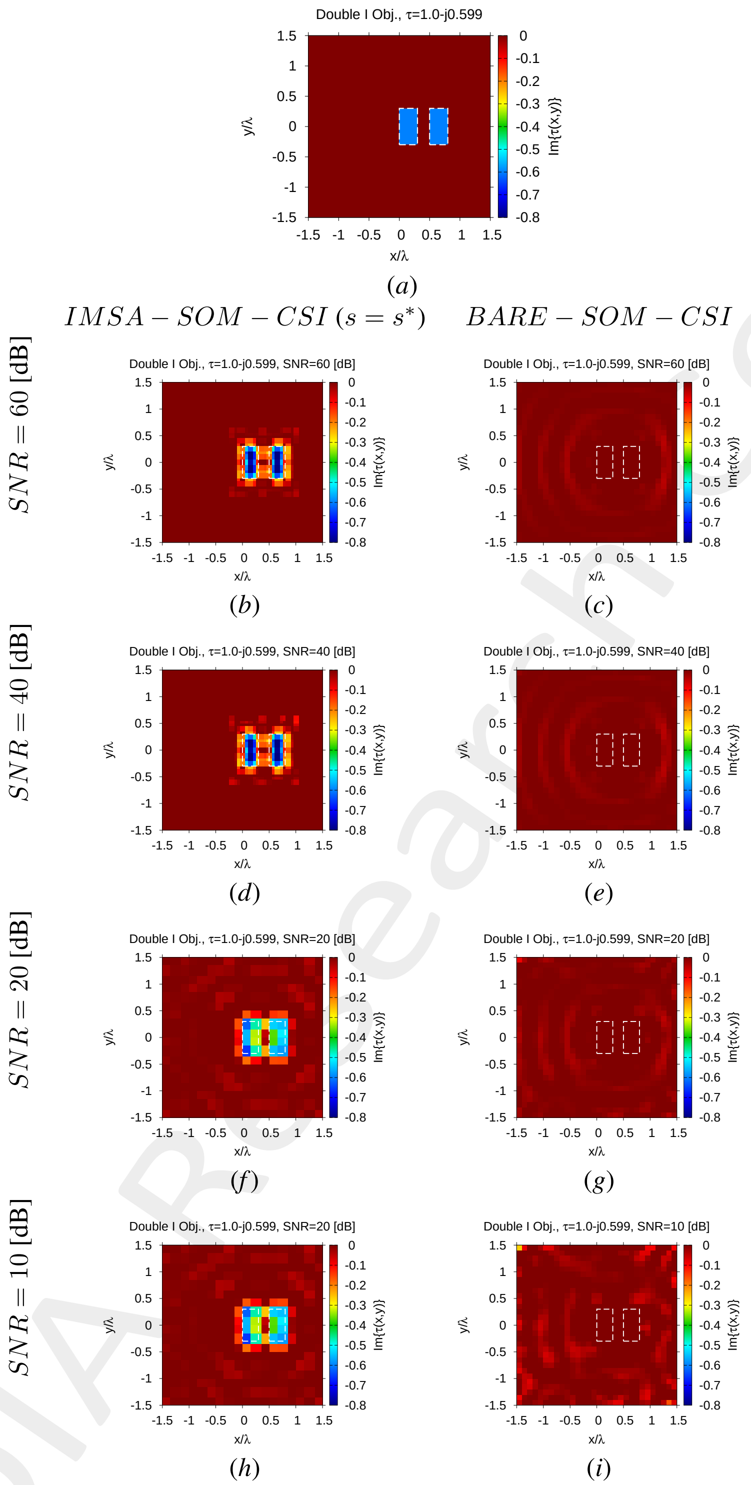

Figure 22: "Double I" Profile, $\tau = 1.0 - j0.6$ - (a) Actual and (b)-(i) retrieved contrast (imaginary part) by the $IMSA-SOM-CSI$ and $BARE-SOM-CSI$ methods under several noise levels.

Reconstruction Errors vs. SNR

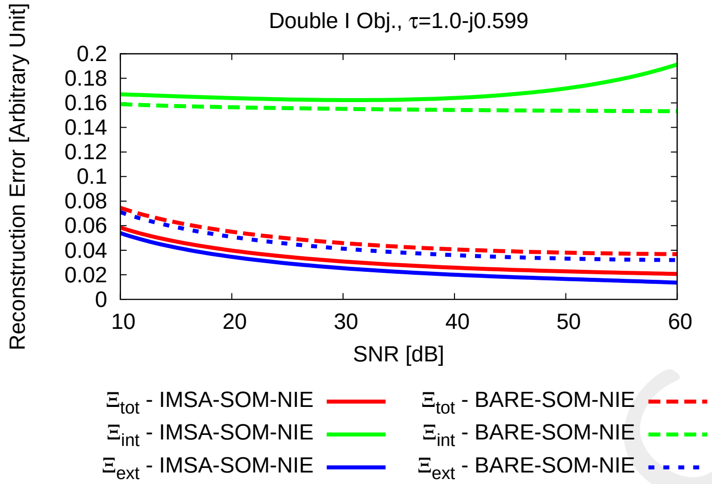

Figure 23: "Double I" Profile, $\tau = 1.0 - j0.6$ - Reconstruction errors for the $IMSA - SOM - NIE$ and $BARE - SOM - NIE$ methods.

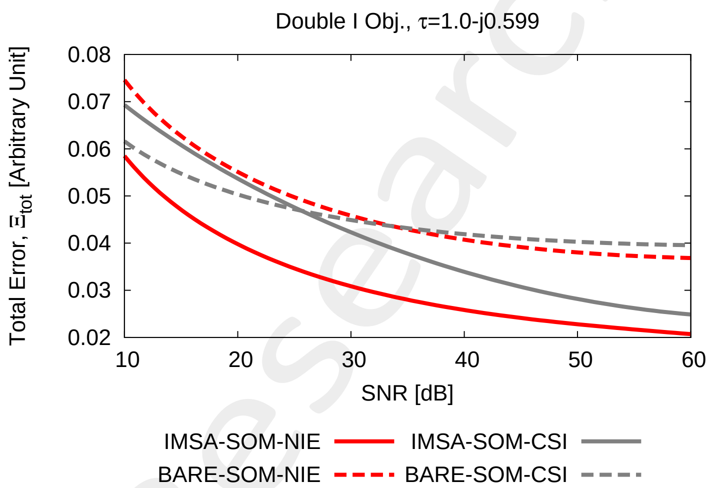

Figure 24: "Double I" Profile, $\tau = 1.0 - j0.6$ - Total error for $IMSA - SOM - NIE$, $BARE - SOM - NIE$, $IMSA - SOM - CSI$, and $BARE - SOM - CSI$.

2.2 Reconstruction Errors vs. σ_{obj}

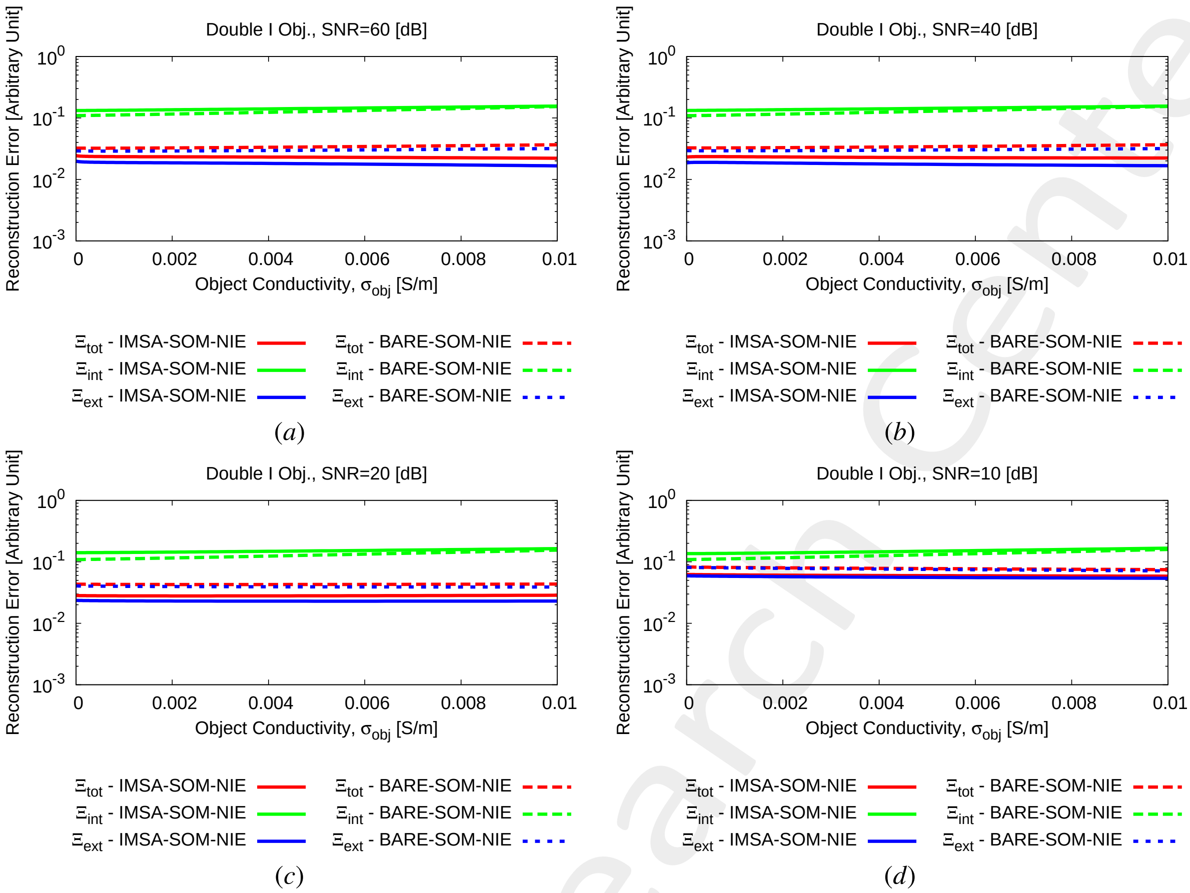

Figure 25: "Double I" Profile - Reconstruction errors vs. $\Re\{\tau\}$ for the $IMSA-SOM-NIE$ and $BARE-SOM-NIE$ methods.

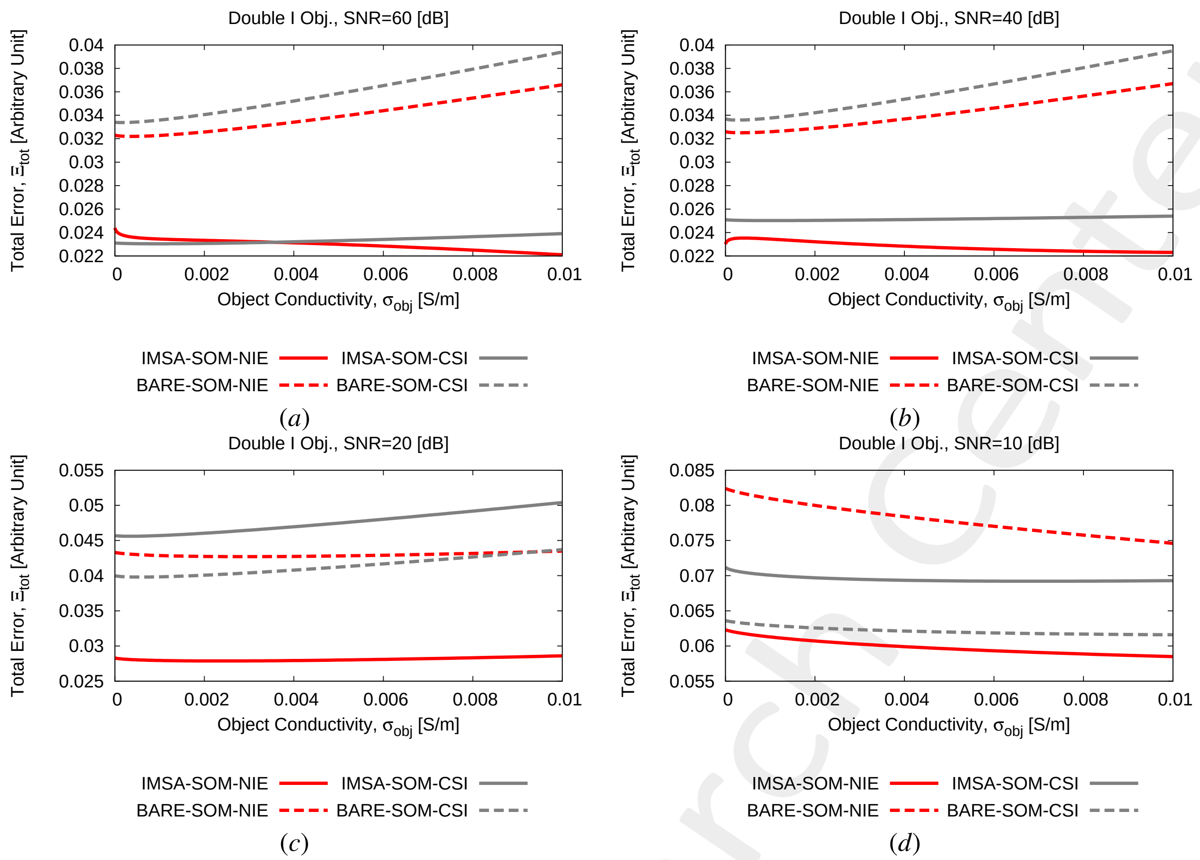

Figure 26: "Double I" Profile - Total error vs. $\Re\{\tau\}$ for $IMSA-SOM-NIE$, $BARE-SOM-NIE$, $IMSA-SOM-CSI$, and $BARE-SOM-CSI$.

2.3 Observations

- In general, the reported results in this section confirm the very good performance of the $IMSA-SOM-NIE$ over state-of-the-art alternatives.

References

[1] G. Oliveri, Y. Zhong, X. Chen, and A. Massa, "Multiresolution subspace-based optimization method for inverse scattering problems," *J. Opt. Soc. Am. A*, vol. 28, no. 10, pp. 2057-2069, Oct. 2011.

[2] X. Ye, L. Poli, G. Oliveri, Y. Zhong, K. Agarwal, A. Massa, and X. Chen, "Multi-resolution subspace-based optimization method for solving three-dimensional inverse scattering problems," *J. Opt. Soc. Am. A*, vol. 32, no. 11, pp. 2218-2226, Nov. 2015.

[3] T. Moriyama, G. Oliveri, M. Salucci, and T. Takenaka, "A multi-scaling forward-backward time-stepping method for microwave imaging," *IEICE Electronics Express*, vol. 11, no. 16, pp. 20140569(1-10), Aug. 2014.

[4] N. Anselmi, G. Oliveri, M. Salucci, and A. Massa, "Wavelet-based compressive imaging of sparse targets," *IEEE Trans. Antennas Propag.*, vol. 63, no. 11, pp. 4889-4900, Nov. 2015.

[5] M. Salucci, G. Oliveri, and A. Massa, "GPR prospecting through an inverse scattering frequency-hopping multi-focusing approach," *IEEE Trans. Geosci. Remote Sens.*, vol. 53, no. 12, pp. 6573-6592, Dec. 2015.

[6] T. Moriyama, M. Salucci, T. Tanaka, and T. Takenaka, "Image reconstruction from total electric field data with no information on incident field," *J. Electromagn. Waves Appl.*, 2016.

[7] M. Salucci, L. Poli, and A. Massa, "Advanced multi-frequency GPR data processing for non-linear deterministic imaging," *Signal Proc.,* vol. 132, pp. 306-318, Mar. 2017.

[8] M. Salucci, L. Poli, N. Anselmi, and A. Massa, "Multifrequency particle swarm optimization for enhanced multiresolution GPR microwave imaging," *IEEE Trans. Geosci. Remote Sens.*, vol. 55, no. 3, pp. 1305- 1317, Mar. 2017.

[9] N. Anselmi, G. Oliveri, M. A. Hannan, M. Salucci, and A. Massa, "Color compressive sensing imaging of arbitrary-shaped scatterers," *IEEE Trans. Microw. Theory Techn.*, vol. 65, no. 6, pp. 1986-1999, Jun. 2017.

[10] G. Oliveri, M. Salucci, N. Anselmi, and A. Massa, "Compressive sensing as applied to inverse problems for imaging: theory, applications, current trends, and open challenges," *IEEE Antennas Propag. Mag.*,vol. 59, no. 5, pp. 34-46, Oct. 2017.

[11] M. Salucci, A. Gelmini, L. Poli, G. Oliveri, and A. Massa, "Progressive compressive sensing for exploiting frequency-diversity in GPR imaging," *J. Electromagn. Waves Appl.*, vol. 32, no. 9, pp. 1164- 1193, 2018.

[12] G. Oliveri, M. Salucci, and N. Anselmi, "Tomographic imaging of sparse low-contrast targets in harsh environments through matrix completion," *IEEE Trans. Microw. Theory Techn.*, vol. 66, no. 6, pp. 2714-2730, Jun. 2018.

[13] M. Salucci, L. Poli, and G. Oliveri, "Full-vectorial 3D microwave imaging of sparse scatterers through a multi-task Bayesian compressive sensing approach," *J. Imaging*, vol. 5, no. 1, pp. 1-24, Jan. 2019.

[14] M. Salucci, G. Oliveri, and A. Massa, "Real-time electrical impedance tomography of the human chest by means of a learning-by-examples method,", *IEEE J. Electromagn., RF, Microw. Med. Biol.*, vol. 3, no. 2, pp. 88-96, Jun. 2019.

[15] G. Oliveri, L. Poli, N. Anselmi, M. Salucci, and A. Massa, “Compressive sensing-based Born iterative method for tomographic imaging,” *IEEE Trans. Microw. Theory Techn.*, vol. 67, no. 5, pp. 1753-1765, May 2019.

[16] I. Merunka, A. Massa, D. Vrba, O. Fiser, M. Salucci, and J. Vrba, "Microwave tomography system for methodical testing of human brain stroke detection approaches," *Int. J. Antennas Propag.,* vol. 2019, ID 4074862, pp. 1-9, 2019.

[17] Y. Zhong, M. Salucci, K. Xu, A. Polo, and A. Massa, “A multi-resolution contraction integral equation method for solving highly non-linear inverse scattering problems,” *IEEE Trans. Microw. Theory Techn.*, vol. 68, no. 4, pp. 1234-1247, Apr. 2020.

[18] M. Salucci, A. Polo, K. Xu, and Y. Zhong, "A multi-resolution computational method to solve highly non-linear inverse scattering problems," *Journal of Physics: Conference Series*, vol. 1476, pp. 1-6, 2020.

[19] N. Anselmi, L. Poli, G. Oliveri, and A. Massa, "Iterative multi-resolution bayesian CS for microwave imaging," *IEEE Trans. Antennas Propag.*, vol. 66, no. 7, pp. 3665-3677, Jul. 2018.

[20] G. Oliveri, P.-P. Ding, and L. Poli "3D crack detection in anisotropic layered media through a sparseness-regularized solver," *IEEE Antennas Wireless Propag. Lett.*, vol. 14, pp. 1031-1034, 2015.

[21] L. Poli, G. Oliveri, P.-P. Ding, T. Moriyama, and A. Massa, “Multifrequency Bayesian compressive sensing methods for microwave imaging," *J. Opt. Soc. Am. A*, vol. 31, no. 11, pp. 2415-2428, 2014.

[22] G. Oliveri, N. Anselmi, and A. Massa, "Compressive sensing imaging of non-sparse 2D scatterers by a total-variation approach within the Born approximation," *IEEE Trans. Antennas Propag.*, vol. 62, no. 10, pp. 5157-5170, Oct. 2014.